Article

Benzene Bridged Carbon Nitride for Efficient Photocatalytic Hydrogen Evolution

Junxia Chu [†], Wencheng Li [†], Zhijun Cao, Xin Bai, Xi Rao *, Shaohui Zheng * and Yongping Zhang *

School of Materials and Energy, Southwest University, Chongqing 400715, China; 1812486728@qq.com (J.C.); 2826268621@qq.com (W.L.); 582170832@qq.com (Z.C.); 2290054173@qq.com (X.B.)

* Corresponding authors. E-mail: raoxiemail@swu.edu.cn (X.R.); shaohuizheng@swu.edu.cn (S.Z.); zhangyyping6@swu.edu.cn (Y.Z.)

[†] These authors contributed equally to this work.

ABSTRACT: Turing the electronic structure by inserting certain functional groups in graphitic carbon nitride (g-C_3N_4, CN for short) skeleton through molecular doping is an effective way to improve its photocatalytic performance. Herein, we prepare a benzene bridged carbon nitride (BCN) by calcining urea and 1,3,5-tribromobenzene at elevated temperature. The introduction of benzene ring in g-C_3N_4 layers improves the separation efficiency and lifetime of photogenerated carriers, inhibits the recombination rate of electron/hole pairs, thus the performance of photocatalytic hydrogen evolution improves. The optimal hydrogen evolution rate of 1.5BCN reaches 1800 μmol/h·g, which is nine times that of the pure g-C_3N_4. DFT calculation proved the benzene bridged CN increased the distance of charge transfer (D_{CT}) and the push-pull electronic effect of intramolecular electrons. This work may provide a pathway for preparing molecular doped g-C_3N_4 with improved photocatalytic performance.

Keywords: Graphitic carbon nitride; Photocatalysis; Hydrogen evolution; Photocatalysts; Molecular design

1. Introduction

Rapid global industrialization results in serious energy shortage and environmental deterioration. Photocatalysis technology provided a promising strategy to deal with energy and environmental issues by converting solar energy into chemical energy directly [1–4]. Designing and developing suitable photocatalysts with high activity, excellent chemical stability and with rich sources has been a hotspot field of photocatalysis. Graphitic carbon nitride (g-C_3N_4) serves as a visible light-driven photocatalyst for solar energy conversion ever since its emergence as a photocatalyst for H_2 evolution from water splitting due to its reasonable energy band structure, high physical and chemical stability, and convenient preparation techniques [5]. Its photocatalytic activity was limited due to its low utilization of visible light, high recombination rate of photogenerated electron/hole pairs and insufficient surface redox reaction sites [6–11]. Certain strategies have been adopted to tackle these shortcomings, such as metal/non-metal element doping [12–14], molecular doping [15–18], heterojunction formation [19–21], morphology construction [22–24], etc. Among them, the introduction of different functional groups through molecular doping to regulate the molecular structure of g-C_3N_4 can optimize the energy band structure and effectively enhance the photocatalytic activity of g-C_3N_4. Recent investigations demonstrated that molecular design is a new pathway to improve its catalytic activity, for example, polymeric carbon nitrides composing of triazine and heptazine unit as building blocks were promising conjugated photocatalysts for hydrogen production from water splitting [25–28].

Common introduced functional groups through molecular doping included aromatic rings, such as benzene ring, pyrimidine, thiophene, etc. Lin et al. synthesized g-C_3N_4 doped with 4,6-dimethyl-2-hydroxypyrimidine (HDMP) through in-situ copolymerization. HDMP doping reduces the band gap, thus promoting the light absorption of g-C_3N_4, and accelerates the transfer of photogenerated electrons as an electron acceptor [29]. Leonard Heyman et al. prepared triazinyl doped g-C_3N_4 molecule by electrochemically polymerizing 2,4,6-triaminopyrimidine (TAP) and melamine molecular, which improved the photocatalytic performance [30]. The introduced C_4N_2 ring changed the electronic structure of CN,

enhanced the mobility of carriers, and improved the photocatalytic activity. Gong et al. covalently grafted pyrene functional group onto the surface of polymerized carbon nitride (PCN) to obtain pyrene functionalized carbon nitride (Py-CN) with excellent photocatalytic activity [31].

Other molecular doping also includes the introduction of carboxyl, hydroxyl, amide groups or other functional groups on the surface of g-C_3N_4. For example, Su et al. prepared carbonyl grafted g-C_3N_4 porous nanosheets with melamine and oxalic acid as precursors, which promoted the separation and transfer of photogenerated electrons and holes, and greatly improved the photocatalytic efficiency [32]. Guo et al. carried out the amidation reaction between 1,2,4,5 phenyltetracarboxylic dianhydride (PMDA) and the –NH_2 group of CN. The introduced anhydride group promoted the separation of photogenerated electrons and holes, and the obtained photocatalyst with stronger photodegradation performance [33].

Among many strategies of molecular doping and introducing functional groups to modify g-C_3N_4, it is a simple and effective way to improve the photocatalytic performance by replacing or doping aromatic rings into the main chain of g-C_3N_4 through π conjugated bonds. The introduced aromatic ring can enhance the visible light response by extending the π conjugation system, and can also promote the separation and transfer of photoexcited charges through the π electronic structure of delocalized g-C_3N_4, so as to obtain higher photocatalytic performance. For example, Li et al. prepared aromatic ring modified g-C_3N_4 nanosheet photocatalyst through copolymerization of urea and aromatic compounds [34]. The introduction of aromatic rings effectively narrowed the band gap, inhibited electron hole recombination, and extended the visible light absorption range. Lin et al. introduced π-electron rich benzene ring in g-C_3N_4 by calcining trimesic acid and melamine [35]. Zhang et al. calcined 2-aminobenzonitrile and dicyandiamide, introduced aromatic ring groups into the CN skeleton, effectively expanded electron delocalization, and improved the photocatalytic performance [17]. Some investigations reported that benzene ring embedded into graphitic carbon nitride facilitated the charge transfer and improved the photocatalytic activity [36,37]. However, there existed inconsistence in the position of benzene ring, such as phenyl ring embedded into the tri-s-triazine framework, as a terminal group, or as a linkage group in CN. More researches were needed to provide more information to understand the molecular structure and its performance. Therefore, we proposed to prepare benzene bridged carbon nitride (BCN) by polymerizing 1,3,5-tribromobenzene and urea at elevated temperature. Through reasonable design, and careful characterization, more information was provided to understand the molecular structure and photocatalytic performance of benzene bridged g-C_3N_4.

Herein, benzene bridged g-C_3N_4 (BCN) was prepared by calcining urea and 1,3,5-tribromobenzene at elevated temperature, introducing benzene ring into g-C_3N_4. The introduction of benzene ring can make the carrier transmission path longer, thus reducing the electron/hole recombination rate. The synergistic effect of mesoporous structure formation and molecular doping on the photocatalytic performance of g-C_3N_4 was evaluated by visible light photocatalytic hydrogen evolution. DFT calculation proved the benzene bridged CN increased the distance of charge transfer (D_{CT}) and the push-pull electronic effect of intramolecular electrons, facilitating the transfer and separation of photogenerated charge carriers.

2. Experimental Details

2.1. Catalyst Preparation

5.0 g of urea was fully dissolved into 50 mL absolute ethanol kept at 80 °C. Then certain amounts of 1,3,5-tribromobenzene (1.0 g, 1.5 g, and 2.0 g) were added into the above-mentioned solution under magnetic stirring to obtain a clear solution. Finally, the solution was dried in an oven at 30 °C for 6 h to get powders, which was calcined in a ceramic boat at 550 °C for 2 h to obtained the benzene bridged carbon nitride, named as 1BCN, 1.5BCN, and 2BCN, respectively. 5 g urea was calcined in a similar process to obtain the pure g-C_3N_4, denoted as CN.

2.2. Catalyst Characterization

X-ray photoelectron spectroscopy (XPS, Thermo Scientific K-alpha, Waltham, MA USA) was carried out to characterize the chemical states of catalysts. The absorption property was measured by a UV-vis diffuse reflectance spectrometer (Agilent Cary 5000 UV-vis NIR, Shanghai, China), using $BaSO_4$ as the reference. The photoluminescence (PL) spectra were recorded on a Hitachi F-7000 spectrophotometer with 150 W xenon light as the excitation source. The transient photocurrent response curve (I−t), and electrochemical impedance spectroscopy (EIS) were performed using an AUTOLAB (model PGSTAT302 N, Herisau, Switzerland) electrochemical workstation. 0.25 M Na_2SO_4 solution was used as the electrolyte and a 500 W xenon lamp as the light source.

2.3. Photocatalytic Reaction

The photocatalytic hydrogen evolution was carried out in a reactor cell connected to sealed gas circulation and evaluation system (Suncat Instrument, Beijing, China). Typically, 10 mg of the photocatalyst was dispersed in 30 mL aqueous solution containing the sacrificial agents 17 vol% triethanolamine (TEOA) and co-catalyst 3 wt% Pt ion ($H_2PtCl_6 \cdot H_2O$), which was continuously stirred during the reaction process. The reactor was evacuated to a high vacuum with pressure of 10^{-8} torr, and then filled with argon, preceding the photocatalytic reaction. Then, the solution was irradiated by a 500 W Xenon lamp (zolix, gloria-x500a, Shenzhen, China) with a 420 nm cut off filter. The light intensity was 113.8 mW cm^{-2} and the light area was 19.6 cm^2. The amount of H_2 production was analyzed by an online gas chromatograph (GC-2018, TCD detector, Shimadzu, Beijing, China) using Ar as carrier. The apparent quantum yield (AQY) of the photocatalysts was calculated according to the light absorption and H_2 evolution rate as follows,

$$AQY(\%) = \frac{\text{number of transfered electron in reaction}}{\text{number of incident photons}} \times 100\% = \frac{2 \times \text{number of evolved } H_2 \text{ molecules}}{\int_{420}^{760} S \times I/E_\lambda} \times 100\%$$

where S is the irradiation area, I is the light intensity, and E_λ is the photon energy with wavelength of λ.

3. Results and Discussion

The crystal structure of the samples was analyzed by X-ray diffraction (XRD). As shown in Figure 1a, for the pure g-C_3N_4, there are two different diffraction peaks at 13.1° and 27.7°, which are respectively attributed to the (100) and (002) crystal planes of g-C_3N_4. After doping 1,3,5-tribromobenzene, the diffraction peak position of the sample has not changed, indicating that the internal structure of the sample remains intact, and the peak intensity just varied slightly, indicating that the stacking of the interlayer structures did not show obvious changes. The FTIR spectra in Figure 1b show that peak at 803 cm^{-1} belongs to the bending vibration absorption of the triazine ring intermediate compound, peak at 1250–1750 cm^{-1} belongs to the stretching vibration of the C–N skeleton structure of the conjugated aromatic ring, and the wide peak at 3000–3400 cm^{-1} belongs to the stretching vibration of the incomplete polycondensation residual ammonia (N–Hx) at the edge of the sample. Benzene ring introduction did not change the structure of graphitic carbon nitride.

Figure 2a depicted that the pure g-C_3N_4 appears as thick stacked sheets at some micrometers. After the doping of benzene ring, the morphology appeared as a porous structure for 1,3,5-tribromobenzene doped g-C_3N_4, as depicted in Figure 2b. TEM image (Figure 2c) of CN appears as curved layers with thickness of 10–20 nm, while catalyst 1.5BCN exhibits as layers with more curvature, as shown in Figure 2d.

The N_2 adsorption-desorption isotherms were illustrated in Figure 2e. The curve shows an obvious H3 hysteresis loop, which is due to the existence of a large number of mesopores in the material. Since the whole synthesis process was carried out at high temperature, this can effectively generate the pore structure of the material, resulting in a significant increase in its specific surface area, which can provide more reaction sites for the photocatalytic reaction, thus facilitating the photocatalytic reaction. The specific surface area of the 1.5BCN sample reached 72 m^2/g, which is larger than the specific surface area of the pure CN of 32 m^2/g. It shows that 1.5BCN sample can provide more active sites in the photocatalytic reaction, which is conducive to enhancing the photocatalytic activity. The corresponding mesoporous distribution of the sample was shown in Figure 2f. It can be seen that the mesoporous size is mainly distributed between 2–5 nm. The mesoporous surface of the material helps to increase the specific surface area of the material and enhance the photocatalytic activity.

X-ray photoelectron spectroscopy (XPS) analysis was carried out to understand the chemical state and chemical composition of the photocatalysts. XPS survey spectra in Figure S1a demonstrated that there appeared the C 1s, N 1s, O 1s signals for CN, 1BCN, 1.5BCN, 2BCN. No Br signals were detected in high-resolution Br 1s spectra for BCN catalysts, as presented in Figure S1b. High-resolution N 1s spectra in Figure 3a can be fitted into three peaks with binding energies at 397.8 eV, 399.1 eV, and 400.2 eV, ascribing to the sp^2 bonded N in C–N=C, the N in N–[C]$_3$, and the N in C–NH_2 [35–39]. The detailed component ration was listed in Table S1. After introducing benzene in CN layer, the ration for N atom in C–NH_2 decreases to 11.5%, 11.1%, 10.8%, for 1BCN, 1.5BCN, and 2BCN, respectively, from 14.1% for CN. That verified that some C–NH_2 groups react with –Br forming linkage C–benzene linkage. High-resolution C 1s spectrum of CN in Figure 1b can be fitted into three peaks with binding energies at 287.5 eV, 285.6 eV, and 284.2 eV. These three peaks are ascribed to the sp^2 hybrid C in N–C=N, the C in C–NH_2, and the adsorbed carbon [36]. Upon inserting benzene ring in CN layer, the peak at 287.5 eV appears obvious broadening in the spectra in Figure 3b, which are decomposed into two peaks, one for the sp^2 bonded N–C=N with binding energy at 287.6 eV, another new peak for benzene at 286.9 eV. The higher binding energy for benzene is due to the formation N–C linkage between

benzene and g-C$_3$N$_4$. This clearly demonstrated that benzene ring is linked to triazine via C–N=C, rather than C–C linkage [36,37]. The component ratio of C 1s peaks is listed in Table 1. The ratio of benzene ring to N–C=N is 24.3%, 36.6%, and 49.1%, for 1BCN, 1.5BCN, and 2BCN, respectively. These results demonstrated that benzene ring was introduced successfully in g-C$_3$N$_4$ molecular structure by N–C linkage.
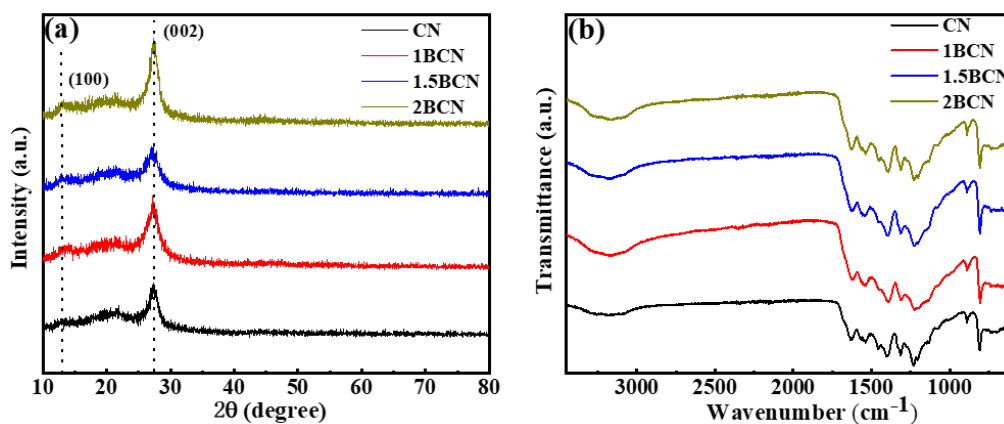

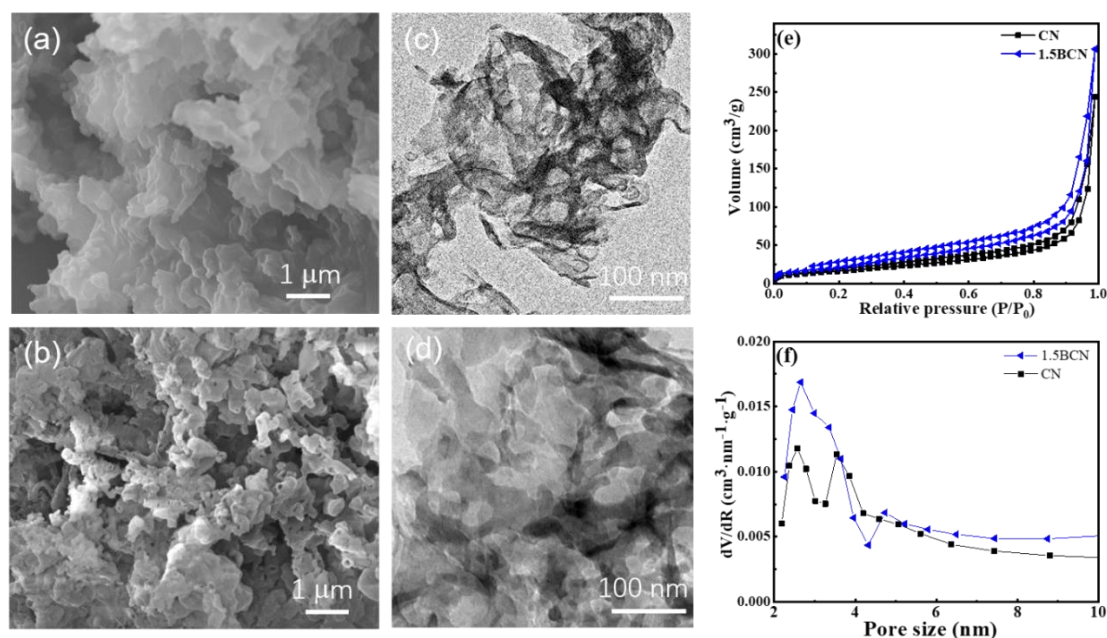**Figure 1.** XRD patterns (**a**) and FTIR spectra (**b**) of pure CN and BCN.

Figure 2. SEM images of pure CN (**a**) and 1.5BCN (**b**). TEM images of pure CN (**c**) and 1.5BCN (**d**). N$_2$ adsorption-desorption isotherms (**e**) and pore distribution (**f**) of CN and 1.5BCN.

Table 1. The Component Ratios of the C 1s Spectra for Different Samples.

Samples	Binding Energy (eV)	Peak Assignment	Atomic Percentage (%)
CN	284.2	adsorbed carbon	48
	285.6	C–NH$_2$	8.8
	287.5	sp^2 bonded N–C=N	43.2
1BCN	284.2	adsorbed carbon	49
	285.6	C–NH$_2$	10.3
	287.6	sp^2 bonded N–C=N	32.7
	286.9	benzene ring	8
1.5BCN	284.2	adsorbed carbon	60.4
	285.6	C–NH$_2$	13
	287.6	sp^2 bonded N–C=N	19.4
	286.9	benzene ring	7.2
2BCN	284.2	adsorbed carbon	50.8
	285.6	C–NH$_2$	11.5
	287.6	sp^2 bonded N–C=N	25.3
	286.9	benzene ring	12.4
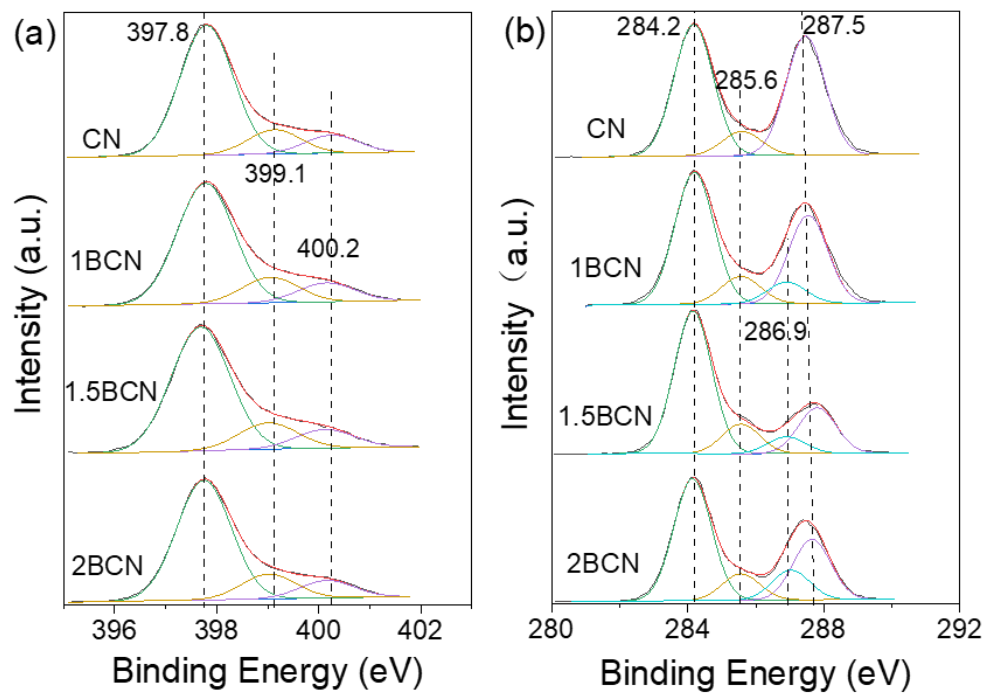
Figure 3. High resolution XPS spectra N 1s (**a**), C 1s (**b**) of CN and BCN.

UV-vis diffuse reflectance spectroscopy (DRS) was measured to characterize the light absorption performance of CN and benzene bridged CN (BCN). As depicted in Figure 4a, the maximum cut-off absorption edge of pure g-C_3N_4 is around 450 nm [40–42]. After the introducing benzene, the light absorption enhanced over an extended visible light range. More light harvestings suggested more electron and hole can be generated under visible light irradiation. Tauc plots converted from UV-vis DRS spectra were shown in Figure 4b. The band gap values of CN, 1BCN, 1.5BCN and 2BCN are estimated to be 2.70 eV, 2.60 eV, 2.52 eV and 2.61 eV respectively. Introducing benzene ring in CN reduced the band gap values slightly, and 1.5BCN with the narrowest band gap among all catalysts.

Mott-schottky measurements in Figure 4c show that the flat-band potential is −1.07 eV and −0.95 eV, for BCN and CN, which indicates that the conduction band is at −1.07 eV and −0.95 eV for BCN and CN, respectively. The valence band can be calculated according the measured bandgap. The band structure is schematically illustrated in Figure 4d. Compared with CN, the BCN with narrowed bandgap and more negative conduction band promotes the photocatalytic efficiency.

Photoelectrochemical measurements are carried out to qualitatively investigate the excitation, transfer and separation characteristics of photogenerated charge carriers in photocatalysts. Figure 5a presents the transient photocurrent response curve recorded for several on-off cycles under visible light irradiation of all catalyst electrodes. At the same bias voltage of 0.8 eV, 1.5BCN exhibits highest photocurrent density among all other samples, about 3.6 times of the photocurrent density of pure CN. That means more electrons can be generated under visible light irradiation for 1.5BCN compared with CN. After five cycles, the photocurrent level does not decline significantly, indicating that the catalyst structure is stable and there is no photoetching phenomenon [43–45]. Figure 5b shows the photocurrent density voltage curve of the original g-C_3N_4 and BCN samples under visible light. Under continuous bias voltage, all samples can respond continuously and stably, and 1.5BCN has the highest photocurrent response among all samples.

Generally, the arc radius on the EIS diagram indicates the charge transfer resistance, and a smaller arc radius means a lower charge transfer resistance. As shown in Figure 5c, the arc radius of EIS of 1.5BCN sample is significantly smaller than that of EIS of other samples, indicating that the interface charge transfer resistance of the electrode obtained after treatment is smaller, which can effectively promote the transport and separation of photogenerated carriers in the catalytic reaction [46,47]. In this paper, photoluminescence spectroscopy tests were used to characterize the effective recombination and instant separation of photoinduced charge carriers. Lower peak intensity means lower recombination rate of free charges and carriers. As shown in Figure 5d, PL spectra exhibit an obvious fluorescence quenching after introducing benzene rings in CN layers [48]. It proved that the recombination rate of photogenerated carriers can be effectively reduced after forming benzene bridged CN, which is conducive to enhancing its ability to photolysis water and hydrogen evolution.

The photocatalytic hydrogen evolution rate of all photocatalysts is shown in Figure 6a. The optimal hydrogen evolution rate of 1.5BCN reached 1800 µmol/h·g, which is about nine times of the pure CN. The average quantum

efficiency (QE) of 1.5BCN reaches 4.82%, much higher than 0.31% of g-C_3N_4. The enhanced factor for the photocatalytic H_2 evolution is better than or comparable to some reported data, as listed in Table 2. In order to verify the stability, 1.5BCN was subjected to a cycle test of hydrogen evolution performance, as shown in Figure 6b. After four cycle tests, the photocatalytic hydrogen production activity did not show obvious changes, indicating that the catalyst can be continuously recycled. XRD patterns of 1.5BCN before and after irradiation did not show obvious changes, indicating the catalyst is stable under visible light irradiation, as depicted in Figure 6c.
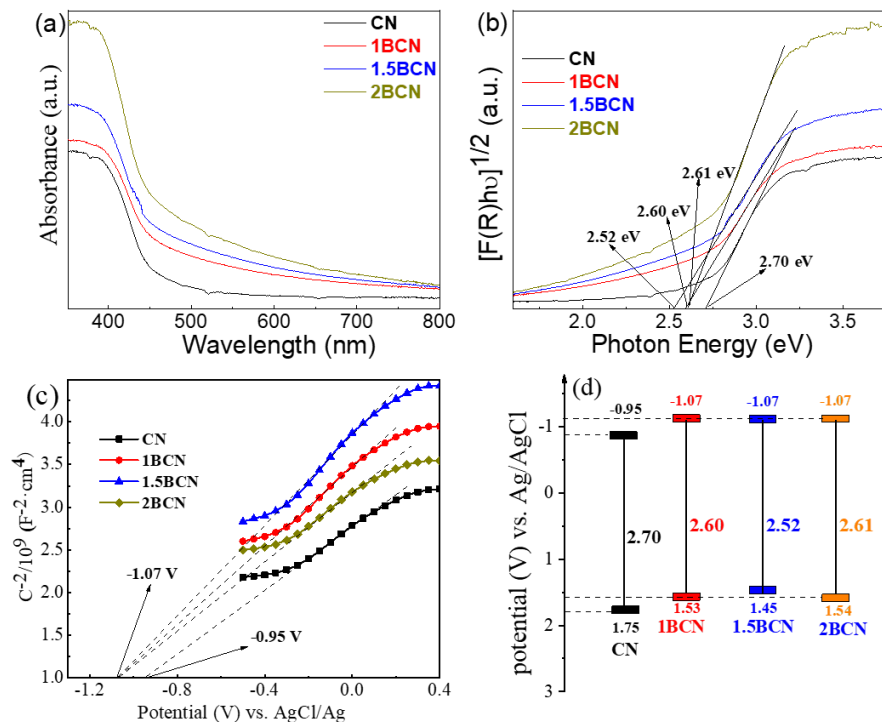
Figure 4. UV-vis diffuse reflectance spectra (**a**), corresponding Kubelka-Munk plots against photo energy (**b**), Mott-Schottky diagram (**c**), and schematic band structure (**d**) of CN, 1BCN, 1.5BCN, and 2BCN.
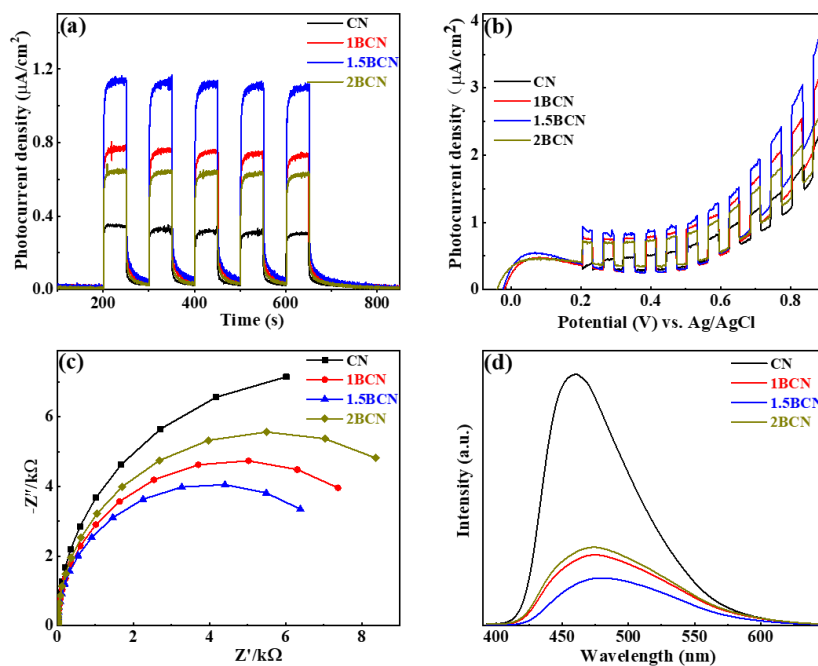
Figure 5. Transient photocurrent response (**a**), photocurrent density-voltage curves (**b**), EIS (**c**), and PL (**d**) of CN and BCN.
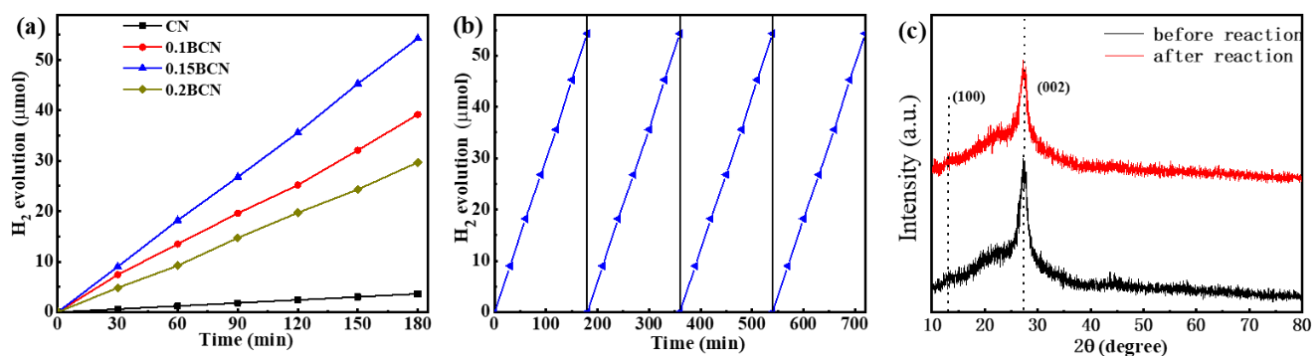
Figure 6. Photocatalytic hydrogen evolution (**a**) of CN, 1BCN, 1.5BCN, 2BCN. Stability test of 1.5BCN (**b**). XRD patterns of 1.5BCN before and after reaction (**c**).

Table 2. Summary of the photocatalytic activities of phenyl doped g-C_3N_4 catalysts.

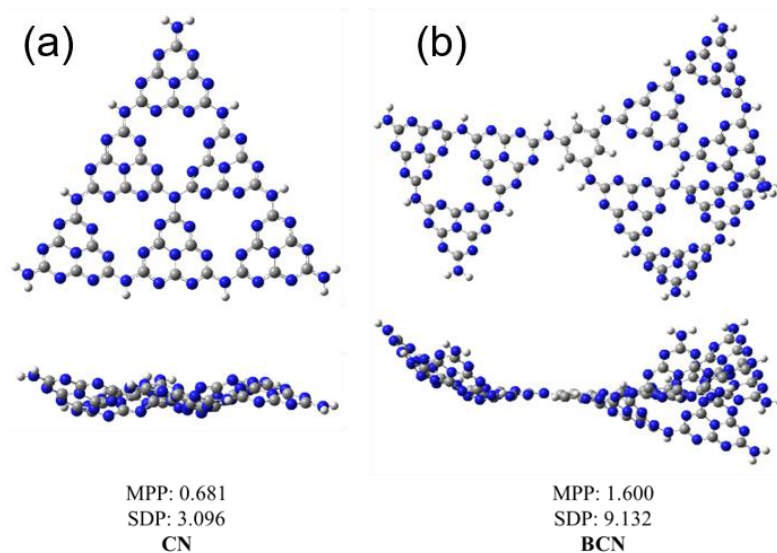| Photocatalyst	Phenyl Sites	H_2 Evolution Rate ($\mu mol\ g^{-1}\ h^{-1}$)	Enhanced Factor [a]	References
Benzene bridged CN	linkage	1931	9.0	this work
Phenyl-doped CN	Terminal group	1470	8.2	[33]
Phenyl-doped CN	embedded in tri-s-triazine framework	2393	2.9	[34]
Phenyl-doped CN	embedded in tri-s-triazine framework	3167	4.0	[35]
Phenyl-doped CN	linkage group	3360	5.4	[36]
Phenyl-doped hollow and porous CN	linkage group	4460	48.4	[37]

[a] Compared with pristine CN.

Based on density functional theory (DFT), Gaussian 09 Version E.01 was used to simulate the electronic structures of CN and BCN. The molecular structural optimization was carried out using M06-2X/def-TZVP theory level. The highest occupied molecular orbital/lowest unoccupied molecular orbital (HOMO/LUMO) was obtained with M06-2X/def2-TZVP theory level. The excited state calculations were performed by using M06-2X/6-311G** for the balance of accuracy and cost. [49] To generate density of states and spin density, we used Multiwfn Rev 3.7 software package [50]. An interesting phenomenon can be found that CN has a structure similar to a "small bowl" after optimization, as shown in Figure 7a. Introducing benzene ring as a linkage via C–N=C in BCN enhances the curvature of the molecular conjugate structure measured by molecular planarity parameter (MPP) and span of deviation from plane (SDP) [51]. Figure 7b demonstrates that the planarity of BCN is worse after the introduction of benzene ring.
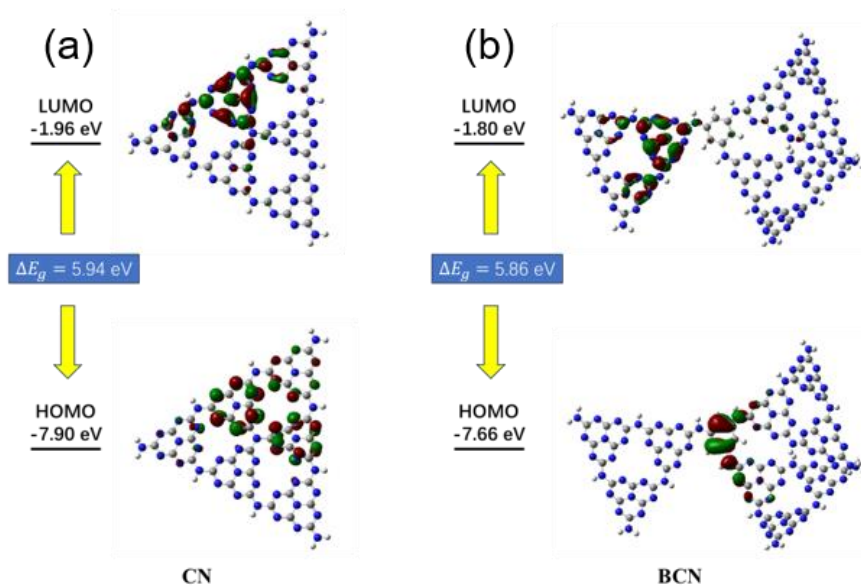
The highest occupied molecular orbital (HOMO) and the lowest unoccupied molecular orbital (LUMO) are calculated to theoretically study the photocatalytic active sites of g-C_3N_4. The HOMO and LUMO of the CN and BCN monolayer (001) crystal planes are shown in Figure 8. The N atom at the edge of the aromatic ring of HOMO (photoexcited hole) of CN provides an oxidation site for oxygen atoms in water, while the C atom at the edge of the aromatic ring and the N atom at the center of the ring of LUMO (photoexcited electron) provide a reduction site for hydrogen ions. The above results indicate that after g-C_3N_4 is excited by light, the electrons on the 2p orbital of the N atom at the edge of the aromatic ring will transition to the 2p orbital of the C atom at the edge of the ring and the N atom at the center of the ring. Because the C atom at the edge of the aromatic ring and the N atom at the center of the ring receive the transition photoelectrons, they are reducible, and can reduce H^+ to H_2, thus conducting the hydrogen evolution reaction. However, the HOMO and LUMO of the pure g-C_3N_4 show an alternating distribution, which leads to the easy recombination of the photogenerated electron hole pairs and short life. After the introduction of benzene ring into BCN, the active sites of HOMO and LUMO change significantly and the degree of delocalization increases, which will help to improve the separation efficiency and lifetime of g-C_3N_4 photogenerated carriers and enhance the photocatalytic reaction. In addition, the introduction of benzene ring significantly reduces the g-C_3N_4 band gap, which is conducive to visible light absorption and promotes visible light catalytic activity. In addition, the small overlap between HOMO and LUMO indicates that BCN has strong charge transfer (CT) characteristics and small electron exchange energy after photo excitation. The dipole moment (1.93 D → 6.95 D) of the molecule can be significantly increased by adding benzene ring, thus increasing the push-pull electronic effect of intermolecular electrons.

As shown in Figure 9, there is small difference between the quantities of intramolecular charge transfer (q_{CT}) of the two structures, indicating that the introduction of benzene ring has little effect on q_{CT}. The introduction of benzene ring can significantly increase the distance of charge transfer (D_{CT}), which means that the charge generated in BCN is not easy to recombine.

Taken the above results into consideration, there exist several factors responsible for the efficient photocatalytic hydrogen evolution of BCN. Firstly, introducing benzene in the g-C_3N_4 results in strong light harvest in visible light range by narrowing band gap, confirmed by UV-vis absorption spectra and DFT calculation. Secondly, the efficient photocatalytic performance can be accredited to the increased specific surface area and pore volume by BCN, and lowered crystallinity, as the N_2 adsorption-desorption isotherms and XRD results, which provide more active sites for photocatalytic reaction. Thirdly, benzene doping resulted in higher photocurrent density, lower EIS and PL intensity, which indicates the efficient transfer and separation of photoinduced charge carriers. DFT calculation confirmed that benzene doping leads to the electron delocalization, longer intramolecular electron transition distance and molecular bending.

Figure 7. Front and side view of optimized structures pure CN (**a**), and BCN (**b**), optimized with M06-2X/def-TZVP theory level.

Figure 8. HOMO, LUMO, and energy gap of CN (**a**), and BCN (**b**), obtained with M06-2X/def2-TZVP theory level. The iso-surface value is set at $0.03e/Bohr^3$. Denotation: C atom-gray, N atom-dark blue.

Figure 9. Electron/hole distributions of the first excited states of CN and BCN, obtained with M06-2X/6-311G** theory level. Intramolecular electron transition distance: D_{ct}; and the intramolecular charge transfer amount: q_{ct}.

4. Conclusions

In conclusion, we prepared benzene bridged g-C_3N_4 photocatalyst (BCN) by calcining 1,3,5-tribromobenzene and urea at elevated temperature, and successfully introduced benzene ring as a linkage in g-C_3N_4 skeleton structure. The introduction of benzene ring improves the separation efficiency and lifetime of photogenerated carriers of g-C_3N_4, reduces the recombination rate of electrons and holes, and improves the efficiency of photocatalytic hydrogen evolution. Under visible light, the photocatalytic hydrogen evolution performance of BCN photocatalyst reached 1800 µmol/h·g, nine times that of pure g-C_3N_4. This work provides a simple and low-cost method for molecular doping to improve the photocatalytic performance of g-C_3N_4.

Supplementary Materials

The following supporting information can be found at: https://www.sciepublish.com/article/pii/106. Additional information including XPS experimental results. DFT calculated total, partial, and overlapped population density of states of CN and BCN.

Acknowledgments

Author Contributions

Investigation, J.C. and W.L.; Original Draft Preparation, J.C.; Writing – Review & Editing, Y.Z.; Visualization, S.Z. and X.R.; Supervision, Y.Z.; Project Administration, X.R.; Funding Acquisition, X.R. and S.Z.; Computation, W.L. and Z.C.; Data curation, J.C. and Z.C.; Validation, S.Z. and Y.Z.; Formal Analysis, S.Z. and Y.Z.; Conceptualization, X.R. and Y.Z.

Ethics Statement

Not applicable.

Informed Consent Statement

Not applicable.

Declaration of Competing Interest

The authors declare no competing financial interest.

References

1. Zhang Y, Yuan S, Feng X, Li H, Zhou J, Wang B. Preparation of Nanofibrous Metal-Organic Framework Filters for Efficient Air Pollution Control. *J. Am. Chem. Soc.* **2016**, *138*, 5785–5788.

2. Guo L, Niu Y, Razzaque S, Tan B, Jin S. Design of D–A1–A2 Covalent Triazine Frameworks via Copolymerization for Photocatalytic Hydrogen Evolution. *ACS Catal.* **2019**, *9*, 9438–9445.

3. Wang B, Wang X, Lu L, Zhou C, Xin Z, Wang J, et al. Oxygen-Vacancy-Activated CO_2 Splitting over Amorphous Oxide Semiconductor Photocatalyst. *ACS Catal.* **2017**, *8*, 516–525.

4. Li B, Fang Q, Si Y, Huang T, Huang WQ, Hu W, et al. Ultra-thin tubular graphitic carbon Nitride-Carbon Dot lateral heterostructures: One-Step synthesis and highly efficient catalytic hydrogen generation. *Chem. Eng. J.* **2020**, *397*, 125479.

5. Wang X, Maeda K, Thomas A, Takanabe K, Xin G, Carlsson JM, et al. A metal-free polymeric photocatalyst for hydrogen production from water under visible light. *Nat. Mater.* **2008**, *8*, 76–80.

6. Zhao S, Fang J, Wang Y, Zhang Y, Zhou Y, Zhuo S. Construction of three-dimensional mesoporous carbon nitride with high surface area for efficient visible-light-driven hydrogen evolution. *J. Colloid Interface Sci.* **2020**, *561*, 601–608.

7. Cheng C, Mao L, Huang Z, Shi J, Zheng B, Zhang Y, et al. Bridging regulation in graphitic carbon nitride for band-structure modulation and directional charge transfer towards efficient H_2 evolution under visible-light irradiation. *J. Colloid Interface Sci.* **2021**, *601*, 220–228.

8. Zhang Y, Huang Z, Dong CL, Shi J, Cheng C, Guan X, et al. Synergistic effect of nitrogen vacancy on ultrathin graphitic carbon nitride porous nanosheets for highly efficient photocatalytic H_2 evolution. *Chem. Eng. J.* **2022**, *431*, 134101.

9. Zhang Y, Huang Z, Shi J, Guan X, Cheng C, Zong S, et al. Maleic hydrazide-based molecule doping in three-dimensional lettuce-like graphite carbon nitride towards highly efficient photocatalytic hydrogen evolution. *Appl. Catal. B Environ.* **2020**, *272,* 119009.

10. Sun N, Liang Y, Ma X, Chen F. Reduced Oxygenated g-C_3N_4 with Abundant Nitrogen Vacancies for Visible-Light Photocatalytic Applications. *Chemistry* **2017**, *23*, 15466–15473.

11. Han Q, Wang B, Gao J, Cheng Z, Zhao Y, Zhang Z, et al. Atomically Thin Mesoporous Nanomesh of Graphitic C_3N_4 for High-Efficiency Photocatalytic Hydrogen Evolution. *ACS Nano* **2016**, *10*, 2745–2751.

12. Fan K, Jin Z, Yang H, Liu D, Hu H, Bi Y. Promotion of the excited electron transfer over Ni- and Co-sulfide co-doped g-C_3N_4 photocatalyst (g-C_3N_4/$Ni_xCo_{1-x}S_2$) for hydrogen Production under visible light irradiation. *Sci. Rep.* **2017**, *7*, 7710.

13. Fao GD, Jiang JC. Theoretical investigation of CO_2 conversion on corrugated g-C_3N_4 surface decorated by single-atom of Fe, Co, and Pd. *Mol. Catal.* **2022**, *526*, 112402.

14. Guo S, Deng Z, Li M, Jiang B, Tian C, Pan Q, et al. Phosphorus-Doped Carbon Nitride Tubes with a Layered Micro-nanostructure for Enhanced Visible-Light Photocatalytic Hydrogen Evolution. *Angew. Chem. Int. Ed.* **2016**, *55*, 1830–1834.

15. Qin J, Wang S, Ren H, Hou Y, Wang X. Photocatalytic reduction of CO_2 by graphitic carbon nitride polymers derived from urea and barbituric acid. *Appl. Catal. B Environ.* **2015**, *179*, 1–8.

16. Zhang J, Chen X, Takanabe K, Maeda K, Domen K, Epping JD, et al. Synthesis of a carbon nitride structure for visible-light catalysis by copolymerization. *Angew. Chem. Int. Ed.* **2010**, *49*, 441–444.

17. Bellamkonda S, Shanmugam R, Gangavarapu R. Extending the π-electron conjugation in 2D planar graphitic carbon nitride: Efficient charge separation for overall water splitting. *J. Mater. Chem. A* **2019**, *7*, 3757–3771.

18. Li Y, Wang S, Chang W, Zhang L, Wu Z, Jin R, et al. Co-monomer engineering optimized electron delocalization system in carbon-bridging modified g-C_3N_4 nanosheets with efficient visible-light photocatalytic performance. *Appl. Cataly. B Environ.* **2020**, *274,* 119116.

19. Chu YC, Lin TJ, Lin YR, Chiu WL, Nguyen BS, Hu C. Influence of P,S,O-Doping on g-C_3N_4 for hydrogel formation and photocatalysis: An experimental and theoretical study. *Carbon* **2020**, *169*, 338–348.

20. Guo F, Shi W, Li M, Shi Y, Wen H. 2D/2D Z-scheme heterojunction of $CuInS_2$/g-C_3N_4 for enhanced visible-light-driven photocatalytic activity towards the degradation of tetracycline. *Sep. Purif. Technol.* **2019**, *210*, 608–615.

21. Yang J, Liang Y, Li K, Yang G, Wang K, Xu R, et al. Cyano and potassium-rich g-C_3N_4 hollow tubes for efficient visible-light-driven hydrogen evolution. *Catal. Sci. Technol.* **2019**, *9*, 3342–3346.

22. Li Y, Zhang D, Fan J, Xiang Q. Highly crystalline carbon nitride hollow spheres with enhanced photocatalytic performance. *Chin. J. Catal.* **2021**, *42*, 627–636.

23. Hong X, Liu Y, Fu J, Wang X, Zhang T, Wang S, et al. A wheat flour derived hierarchical porous carbon/graphitic carbon nitride composite for high-performance lithium–sulfur batteries. *Carbon* **2020**, *170*, 119–126.

24. Yin JT, Li Z, Cai Y, Zhang QF, Chen W. Ultrathin graphitic carbon nitride nanosheets with remarkable photocatalytic hydrogen production under visible LED irradiation. *Chem. Commun.* **2017**, *53*, 9430–9433.

25. Liu M, Zhang G, Liang X, Pan Z, Zheng D, Wang S, et al. Rh/Cr_2O_3 and CoO_x cocatalysts for efficient photocatalystic water splitting by poly(triazine imide) crystals. *Angew. Chem. Int. Ed.* **2023**, *62*, e202304694.

26. Zhang J, Ye G, Zhang C, Pan Z, Wang S, Zhang G, et al. Heptazine-based ordered-disordered copolymers with enhanced visible-light absorption for photocatalytic hydrogen production. *ChemSusChem* **2022**, 15, e202201616.

27. Chang M, Pan Z, Zheng D, Wang S, Zhang G, Anpo M, et al. Salt-melt synthesis of poly heptazine imide with enhanced optical absorption for photocatalytic hydrogen production. *ChemSusChem* **2023**, *16*, e202202255.

28. Wang Q, Zhang G, Xing W, Pan Z, Zheng D, Wang S, et al. Bottom-up synthesis of single-crystalline poly (triazine imide) nanosheets for photocatalytic overall water splitting. *Angew. Chem. Int. Ed.* **2023**, *62*, e202307930.

29. Lin Y, Wang L, Yu Y, Zhang X, Yang Y, Guo W, et al. Construction of molecularly doped and cyano defects co-modified graphitic carbon nitride for the efficient photocatalytic degradation of tetracycline hydrochloride. *New J. Chem.* **2021**, *45*, 18598–18608.

30. Heymann L, Bittinger SC, Klinke C. Molecular Doping of Electrochemically Prepared Triazine-Based Carbon Nitride by 2,4,6-Triaminopyrimidine for Improved Photocatalytic Properties. *ACS Omega* **2018**, *3*, 17042–17048.

31. Gong X, Yu S, Guan M, Zhu X, Xue C. Pyrene-functionalized polymeric carbon nitride with promoted aqueous–organic biphasic photocatalytic CO_2 reduction. *J. Mater. Chem. A* **2019**, *7*, 7373–7379.

32. Su FY, Zhang WD. Carbonyl-Grafted g-C_3N_4 Porous Nanosheets for Efficient Photocatalytic Hydrogen Evolution. *Chem.-Asian J.* **2017**, *12*, 515–523.

33. Zhang J, Zhang G, Chen X, Lin S, Mohlmann L, Dolega G, et al. Co-monomer control of carbon nitride semiconductors to optimize hydrogen evolution with visible light. *Angew. Chem. Int. Ed.* **2012**, *51*, 3183–3187.

34. Yu Y, Yan W, Gao W, Li P, Wang X, Wu S, et al. Aromatic ring substituted g-C_3N_4 for enhanced photocatalytic hydrogen evolution. *J. Mater. Chem. A* **2017**, *5*, 17199–17203.

35. Lin X, Hou X, Cui L, Zhao S, Bi H, Du H, et al. Increasing π-electron availability in benzene ring incorporated graphitic carbon nitride for increased photocatalytic hydrogen generation. *J. Mater. Sci. Technol.* **2021**, *65*, 164–170.

36. Chen Y, Qu Y, Zhou X, Li D, Xu P, Sun J. Phenyl-bridged graphitic carbon nitride with a porous and hollow sphere structure to enhance dissiciation of photogenerated charge carriers and visible-light-driven H_2 generation. *ACS Appl. Mater. Interfaces* **2020**, *12*, 41527–41537.

37. Yuan H, Bai J, Xu B, Li X, Xiao S, Liu P, et al. Graphitic carbon nitride doped with a benzene ring for enhanced photocatalytic H_2 evolution. *Chem. Commun.* **2021**, *57*, 3042–3045.

38. Chen P, Lei B, Dong X, Wang H, Sheng J, Cui W, et al. Rare-Earth Single-Atom La-N Charge-Transfer Bridge on Carbon Nitride for Highly Efficient and Selective Photocatalytic CO_2 Reduction. *ACS Nano* **2020**, *14*, 15841–15852.

39. Chen L, Man Y, Chen Z, Zhang Y. Ag/g-C_3N_4 layered composites with enhanced visible light photocatalytic performance. *Mater. Res. Express* **2016**, *3*, 115003.

40. Gao D, Liu Y, Liu P, Si M, Xue D. Atomically Thin B doped g-C_3N_4 Nanosheets: High-Temperature Ferromagnetism and calculated Half-Metallicity. *Sci. Rep.* **2016**, *6*, 35768.

41. Wang X, Chen X, Thomas A, Fu X, Antonietti M. Metal-Containing Carbon Nitride Compounds: A New Functional Organic-Metal Hybrid Material. *Adv. Mater.* **2009**, *21*, 1609–1612.

42. Fang J, Fan H, Li M, Long C. Nitrogen self-doped graphitic carbon nitride as efficient visible light photocatalyst for hydrogen evolution. *J. Mater. Chem. A* **2015**, *3*, 13819–13826.

43. Bledowski M, Wang L, Ramakrishnan A, Khavryuchenko OV, Khavryuchenko VD, Ricci PC, et al. Visible-light photocurrent response of TiO$_2$-polyheptazine hybrids: evidence for interfacial charge-transfer absorption. *Phys. Chem. Chem. Phys.* **2011**, *13*, 21511–21519.

44. Li J, Shen B, Hong Z, Lin B, Gao B, Chen Y. A facile approach to synthesize novel oxygen-doped g-C_3N_4 with superior visible-light photoreactivity. *Chem. Commun.* **2012**, *48*, 12017–12019.

45. Liang Q, Li Z, Bai Y, Huang ZH, Kang F, Yang QH. A Composite Polymeric Carbon Nitride with In Situ Formed Isotype Heterojunctions for Highly Improved Photocatalysis under Visible Light. *Small* **2017**, *13*, 1603182.

46. Li L, Yan J, Wang T, Zhao ZJ, Zhang J, Gong J, et al. Sub-10 nm rutile titanium dioxide nanoparticles for efficient visible-light-driven photocatalytic hydrogen production. *Nat. Commun.* **2015**, *6*, 5881.

47. Yao C, Yuan A, Wang Z, Lei H, Zhang L, Guo L, et al. Amphiphilic two-dimensional graphitic carbon nitride nanosheets for visible-light-driven phase-boundary photocatalysis. *J. Mater. Chem. A* **2019**, *7*, 13071–13079.

48. Kim H, Gim S, Jeon TH, Kim H, Choi W. Distorted Carbon Nitride Structure with Substituted Benzene Moieties for Enhanced Visible Light Photocatalytic Activities. *ACS Appl. Mater. Interfaces* **2017**, *9*, 40360–40368.

49. Frisch MJ, Trucks GW, Schlegel HB, Scuseria GE, Robb MA, Cheeseman JR, et al. *Gaussian 09*, Revision E.01; Gaussian, Inc.: Wallingford, CT, USA, 2013.

50. Lu T, Chen F. Multiwfn: a multifunctional wavefunction analyzer. *J. Comput. Chem.* **2012**, *33*, 580–592.

51. Lu T. Simple, reliable, and universal metrics of molecular planarity. *J. Mol. Model.* **2021**, *27*, 263.